


# Effect of Temperature on Tribological Behavior of FeCrNi Medium Entropy Alloy

Ao Fu <sup>1</sup>, Zhonghao Xie <sup>1</sup>, Weiwei He <sup>2,\*</sup> and Yuankui Cao <sup>1,3,\*</sup> <sup>1</sup> State Key Laboratory of Powder Metallurgy, Central South University, Changsha 410083, China<sup>2</sup> Xi'an Sailong AM Technologies Co., Ltd., Xi'an 710019, China<sup>3</sup> Foshan (Southern China) Institute for New Materials, Foshan 528010, China

\* Correspondence: hewi126@126.com (W.H.); caoyuankui@csu.edu.cn (Y.C.)

**Abstract:** FeCrNi medium entropy alloy (MEA) is a promising structural material due to its outstanding mechanical properties and corrosion resistance. However, study on the high-temperature tribological behaviors of FeCrNi MEA is still scarce. This work investigates the tribological performances of the FeCrNi MEA against Si<sub>3</sub>N<sub>4</sub> balls over typical operating temperatures from 25 to 800 °C. The FeCrNi MEA exhibits excellent wear resistance at an intermediate temperature of 600 °C. The microstructure characterization of the wear tracks reveals a transition in the wear mechanism from abrasive wear at 25 °C to oxidative-delamination wear at 600 °C. The improved tribological performances are mainly attributed to the high Cr content, which promotes the formation of the compact oxide layer and the precipitation of the hard sigma ( $\sigma$ ) phase.

**Keywords:** medium entropy alloys; powder metallurgy; tribological property; precipitation strengthening



**Citation:** Fu, A.; Xie, Z.; He, W.; Cao, Y. Effect of Temperature on Tribological Behavior of FeCrNi Medium Entropy Alloy. *Metals* **2023**, *13*, 282. <https://doi.org/10.3390/met13020282>

Academic Editors: Petra Maier and Normen Fuchs

Received: 30 December 2022

Revised: 28 January 2023

Accepted: 29 January 2023

Published: 31 January 2023



**Copyright:** © 2023 by the authors. Licensee MDPI, Basel, Switzerland. This article is an open access article distributed under the terms and conditions of the Creative Commons Attribution (CC BY) license (<https://creativecommons.org/licenses/by/4.0/>).

## 1. Introduction

Fe-Cr-Ni series stainless steels, e.g., 304 and 316, have become the fundamental anti-corrosion material for marine engineering due to their outstanding mechanical properties and corrosion resistance [1,2]. The high Cr content in the stainless steels can promote the formation of a protective oxide layer on the surface of the alloys, which is beneficial to inhibit pitting corrosion in harsh environments [3,4]. However, when the Cr content in the stainless steels is higher than 25 wt.%, a hard but brittle sigma ( $\sigma$ ) phase can form, leading to deterioration in ductility and corrosion resistance [5,6]. Therefore, how to break the limitation of the Cr content with reasonable regulation of the  $\sigma$ -phase precipitation and achieve enhanced comprehensive performance remains a critical challenge.

Recently, a brand-new design strategy of medium/high entropy alloys (MEAs/HEAs) has provided new sight for the development of high-performance anti-corrosion materials. MEAs/HEAs are composed of multiple principal elements in equimolar or near-equimolar ratios, and the high mixing entropy enables these alloys to form simple solid solution structures, such as face-centered cubic (FCC) and body-centered cubic (BCC), instead of complex phases and intermetallic compounds [7–9]. Based on the MEAs/HEAs concept, a novel high Cr single-phase FCC FeCrNi MEA was first developed by Wu et al. [10], and many recent literatures have investigated its microstructure and basic mechanical properties. For instance, Wang et al. [11] fabricated the FeCrNi MEA by vacuum arc melting and cold rolling. The yield strength (YS) and ultimate tensile strength (UTS) reach 260 MPa and 580 MPa, respectively. Duan et al. [12] prepared the FeCrNi MEA via selective laser melting (SLM) and found that the alloy exhibits an excellent combination of strength ( $\sigma_{YS} = 745$  MPa,  $\sigma_{UTS} = 1007$  MPa) and ductility ( $\epsilon_f = 31\%$ ). Schneider et al. [13] studied the effect of temperature on the mechanical properties of the FeCrNi MEA and declared that the alloy has enhanced strength and ductility at low temperature. Liang et al. [14] fabricated the ultrafine-grained FeCrNi MEA via mechanical alloying and spark plasma sintering

(SPS), and its hardness at room temperature (RT) could reach ~267 HV. A further study reported by Zhou et al. [15] suggests that the FeCrNi MEA exhibits desirable corrosion resistance in 3.5 wt.% NaCl solution compared with the 316L SS.

Wear is an inevitable phenomenon in our daily life and production. Due to the above attractive properties of the FeCrNi MEA, such as balanced strength and ductility as well as outstanding corrosion resistance [15,16], the research on its tribological properties becomes an interesting topic. Nevertheless, to date, few studies are available in the literatures in terms of the wear behavior of the FeCrNi MEA, especially at high temperature. Herein, we prepared a representative FeCrNi MEA via the powder metallurgy method, and we focused on its temperature-dependent tribological behavior and wear mechanism from RT to 800 °C.

## 2. Materials and Methods

High-purity (99.99%) spherical FeCrNi MEA powders were prepared by the gas atomization method and then extruded to a bar via a 2500 T hydraulic press. The extrusion ratio and temperature are 7:1 and 1150 °C, respectively. The details of the preparation process and parameters have been described in our previous work [16]. The chemical composition of the extruded bar was analyzed to be Fe<sub>33.7</sub>Cr<sub>33.7</sub>Ni<sub>32.5</sub> (at.%).

Chemical composition was determined by the inductively coupled plasma mass spectrometry (ICP-MS) analysis (Thermo Fisher, Waltham, MA, USA). Phase identification was determined by an X-ray diffractometer (XRD, Advance D8, Bruker, Karlsruhe, Germany) equipped with a Cu  $K\alpha$  radiation. Microstructure characterization was examined by a scanning electron microscopy (SEM, Helios G3 UC, FEI, Brno, Czech Republic) equipped with energy dispersive spectrometer (EDS) instrument. Tribological tests were carried out on a HT-1000 ball-on-disk tribometer (ZhongkeKaihua, Lanzhou, China) at RT, 600 and 800 °C, respectively. Top Si<sub>3</sub>N<sub>4</sub> balls with a diameter of 3 mm were utilized as counter-part materials. The applied load, sliding velocity and testing time were 10 N, 0.084 m/s and 30 min, respectively. Each test was repeated at least three times to ensure the accuracy of the data. The volumetric loss was evaluated from three-dimensional (3D) optical profilometer (VHX-5000, Keyence, Osaka, Japan). The wear rate was calculated by the formula:  $\omega = V/SL$ , where  $\omega$ ,  $S$  and  $L$ , represent the wear volume, the sliding distance and the normal load, respectively. Wear surfaces were examined by SEM and EDS. Chemical compounds of the wear surfaces were determined by an X-ray photoelectron spectroscopy (XPS, Escalab 250, Thermo Fisher, MA, USA).

## 3. Results and Discussion

### 3.1. Phase Constitution and Microstructure

Figure 1a shows the XRD patterns of the FeCrNi MEA. It can be seen that the diffraction peaks of the FeCrNi MEA are identified to be a single-phase FCC solid solution. This meant that the FeCrNi MEA did not undergo phase transformation during hot extrusion. Figure 1b gives the typical inverse pole figure (IPF) map of the FeCrNi MEA, and the equiaxed grain with a diameter of ~12  $\mu\text{m}$  is obtained. The existence of numerous annealing twins in the grain interior indicates that the stacking fault energy (SFE) of the FeCrNi MEA is low, and a similar phenomenon has been also found in many FCC HEAs/MEAs [17]. Figure 1c shows the EDS mappings of Fe, Cr and Ni elements in the FeCrNi MEA. Clearly, all elements are almost randomly distributed. Additionally, there are no other detectable intermetallic compounds or elemental segregation.

### 3.2. Tribological Performance

Figure 2a shows the friction coefficient versus the sliding time for the FeCrNi MEA at temperatures from RT to 800 °C. As indicated, the surface friction coefficient of the FeCrNi MEA at RT increases gradually until a steady state is reached due to the breaking of the wear surface and the settling down of the indenter, exhibiting a high friction coefficient of ~0.67. The friction coefficient is calculated from the data in the last two thirds of the friction

coefficient curve. With the increase of temperature, the friction coefficient of the FeCrNi MEA is negatively correlated with the test temperatures (Figure 2b) and drops rapidly to 0.44 at 800 °C. The dropping of friction coefficient with increased temperature could be attributed to the formation of compact oxide layers on the wear surface and low adhesive force at the contact interface [18,19]. The oxide layer can make the inter-atomic binding force between the friction pairs be replaced by the weaker Van der Waals forces, which helps to reduce the friction coefficient [19,20]. The microstructure characterization of the oxide layer will be discussed later. The adhesion force is very sensitive to temperature and will decrease with the increase of test temperature [21], which is also responsible for the decline of the friction coefficient at high temperature.

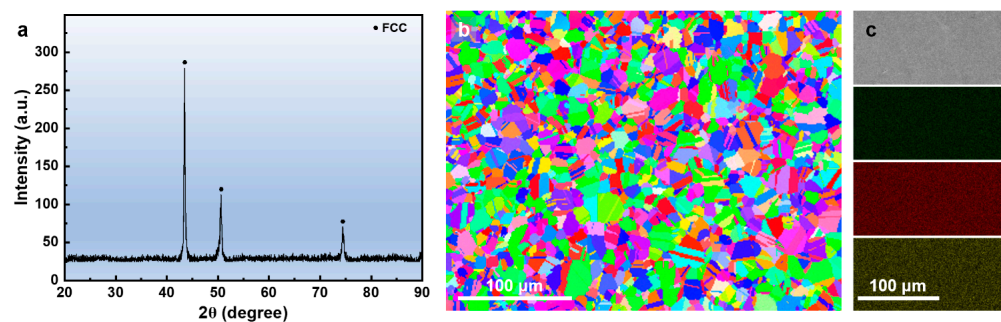


Figure 1. (a) XRD pattern, (b) EBSD IPF map and (c) EDS elemental distribution of the FeCrNi MEA.

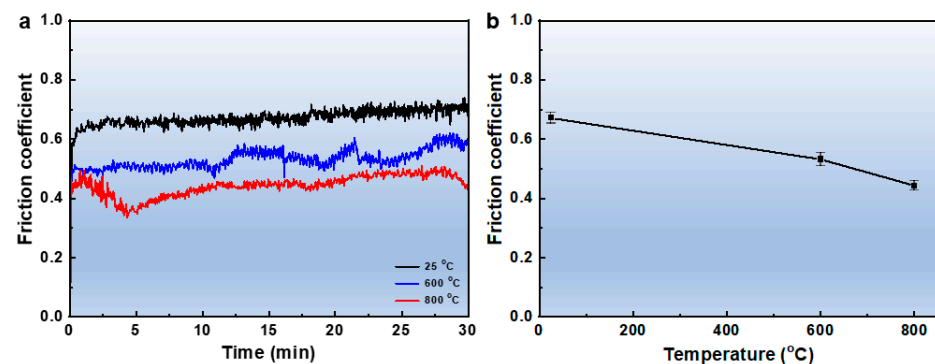
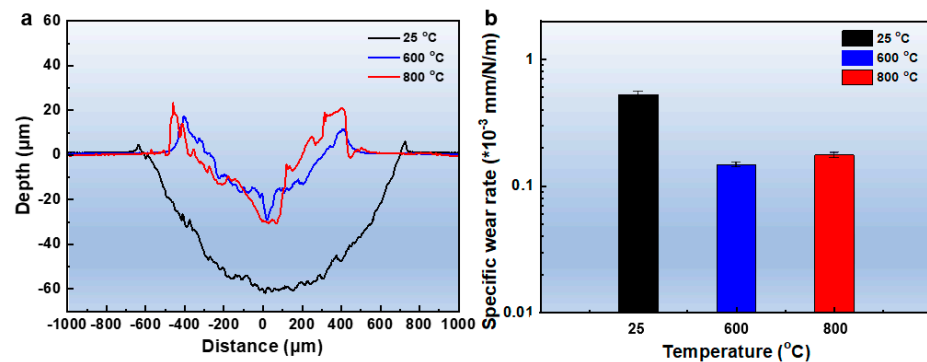


Figure 2. (a) Friction coefficient as a function of the sliding time for the FeCrNi MEA under different test temperatures; (b) variations of the friction coefficient with the test temperatures.

Figure 3a shows the 2D cross-section depth profile of the wear tracks of the FeCrNi MEA at temperatures from RT to 800 °C. It can be seen that the wear tracks are narrower and shallower at 600 °C and 800 °C compared to RT. Wear rate is usually used to evaluate wear resistance, and a lower wear rate stands for a higher wear resistance [22]. Figure 3b summarizes the corresponding wear rates at various temperatures. The wear rate of the FeCrNi MEA is  $\sim 5.3 \times 10^{-5} \text{ mm}^3/\text{Nm}$  at RT, which decreases to the minimum value at 600 °C and then increases slightly as the test temperature rises to 800 °C. A similar intermediate temperature strengthening phenomenon is observed in the CoCrFeMnNi HEA and  $\text{Al}_{0.6}\text{CoCrFeNi}$  HEA, showing enhanced wear resistance at intermediate temperatures from 400 °C to 700 °C [23]. The relatively low wear rate at intermediate temperature for the MEA/HEA can be attributed to the formation of compact oxide layers and the precipitation of hard second-phase particles on the wear surface, which is beneficial to withstand the abrasions. The chemical composition of the FeCrNi MEA is significantly different from the typical CoCrFeMnNi HEA and  $\text{Al}_{0.6}\text{CoCrFeNi}$  HEA, and the wear behavior is bound to be different. To understand the wear behavior of the FeCrNi MEAs as a function of temperature, more investigations on the wear surfaces after sliding are badly needed.



**Figure 3.** (a) The cross-section depth profiles of the wear tracks under different test temperatures; (b) the corresponding wear rate histograms.

### 3.3. Tribological Performance

Figure 4 shows the 3D optical profilometer and secondary electron (SE) images of the wear tracks of the FeCrNi HEA, tested at temperatures from RT to 800 °C. The FeCrNi MEA wears uniformly at RT with relatively wide and deep wear tracks (Figure 4a,b), and the wear surface is flooded with fine grooves, scattered wear debris and narrow microcracks, demonstrating that abrasive wear was the dominant wear mechanism. Cyclic friction can induce temperature increasing on the wear surface, which leads to oxidation and cracking on the surface, resulting in wear debris. From the EDS results in Table 1, it can be seen that the wear debris is mainly oxides, containing various elements such as Fe, Cr, Ni and O. Significant differences in the morphology of the wear tracks can be observed as the test temperature changes. At 600 °C, the width and depth of the wear track decreases significantly (Figure 4c,d), showing improved wear resistance. The wear tracks exhibit periodic valleys and mounds along the sliding direction, which becomes more apparent at 800 °C (Figure 4e). This phenomenon has been previously observed in alloys with low hardness at high operating temperatures because of surface deformation and plastic flow close to the subsurface region [23,24]. Figure 4d,f shows the high-magnification surface morphologies tested at 600 °C and 800 °C, respectively. The wear surface at high temperature is different from that at RT, showing a lamellar morphology with some localized microcracks. The oxygen content of the wear surface increases significantly (Table 1), because the degree of oxidation reaction is increased with increasing the environmental temperature. A smooth and complete oxide layer enriched with Cr and O elements formed on the wear surface, which is similar to previous research results [23]. The low shear strength and high hardness of the oxide layer help to obtain a low friction coefficient. At the same time, the oxide layer can prevent the direct contact between friction pairs and helps to reduce abrasive wear and adhesive wear. Therefore, the wear mechanism gradually changes from abrasive wear at RT to oxidative and delamination wear at high temperature.

High temperatures can induce the formation of the oxide layer, thereby affecting the tribological performance. To understand the wear mechanism more clearly, the cross-section morphologies and chemical compositions of the wear tracks for the FeCrNi MEA at 600 °C and 800 °C are systematically characterized as shown in Figure 5. At 600 °C, a dense and continuous oxide layer with a thickness of up to ~5.75 μm can be clearly seen. EDS analysis shows that the oxide layer is mainly composed of Cr and O elements. Since the formation enthalpy of Cr oxide ( $\Delta H_{\text{Cr}_2\text{O}_3} = -1139$  kJ/mol) is lower than that of Fe oxide ( $\Delta H_{\text{Fe}_2\text{O}_3} = -825$  kJ/mol) and Ni oxide ( $\Delta H_{\text{NiO}} = -241$  kJ/mol,  $\Delta H_{\text{Ni}_2\text{O}_3} = -450$  kJ/mol), the content of Cr in the oxide films of the FeCrNi MEA is higher. EDS results at high magnifications indicate that there are numerous fine, Cr-rich,  $\sigma$ -phase precipitates in the oxide layer (Figure 5e), and these particles are able to produce significant precipitation strengthening and improve surface strength. According to the equilibrium phase diagram, the FeCrNi MEA has a single-phase FCC structure above 1223 K, and the  $\sigma$  phase will gradually precipitate when the operating temperature is lower than 1223 K [13]. At the

same time, thermomechanical deformation on the surface of the FeCrNi MEA during the friction process can promote the precipitation of the  $\sigma$  phase. Previous studies have shown that the formation of the  $\sigma$  phase leads to enhanced strength of the VCoCrFeMnNi HEA [25] and improved wear resistance of the CoCrFeMnNi HEA [23,26] under high temperature. The MEAs/HEAs containing Cr usually precipitate a low-volume  $\sigma$  phase after long-term annealing at intermediate temperatures, and the  $\sigma$  phase will further evolve into nanoscale precipitates after severe deformation [23,25–27]. In addition, the structure and valent states of the elements on the wear surface is detected by XPS analysis, as shown in Figure 6. The wear surface is composed of multi-type of oxides, such as  $\text{Fe}_2\text{O}_3$ ,  $\text{Cr}_2\text{O}_3$ ,  $\text{NiCr}_2\text{O}_4$  and  $\text{Ni}_x\text{O}_y$ , in which lubricious metal oxides ( $\text{NiO}$ ,  $\text{Ni}_2\text{O}_3$  and  $\text{NiO}_x$ ) and inorganic acid salts ( $\text{NiCr}_2\text{O}_4$ ) prefer to form at higher temperature and are beneficial to promote the formation of the compact oxide layer, therefore reducing the friction coefficient. When the friction temperature reaches  $800^\circ\text{C}$ , the wear surface of the FeCrNi MEA is also covered with a protective oxide layer, and the chemical composition of the oxide film is similar to that at  $600^\circ\text{C}$ . However, the thickness of the oxide layer decreases slightly with the increase of temperature and fluctuates around  $4.61\ \mu\text{m}$ . The cracks, voids and micro-pits are presented on the wear surface, which may be due to surface fatigue and shear instability during cyclic contact stress. Meanwhile, the size of the second phase becomes larger. The phenomenon that the volume fraction of the  $\sigma$  phase increases and the size becomes larger is also observed in the FeCoCrNiMn HEA [26]. This could be the reason for the slightly increased wear rate.

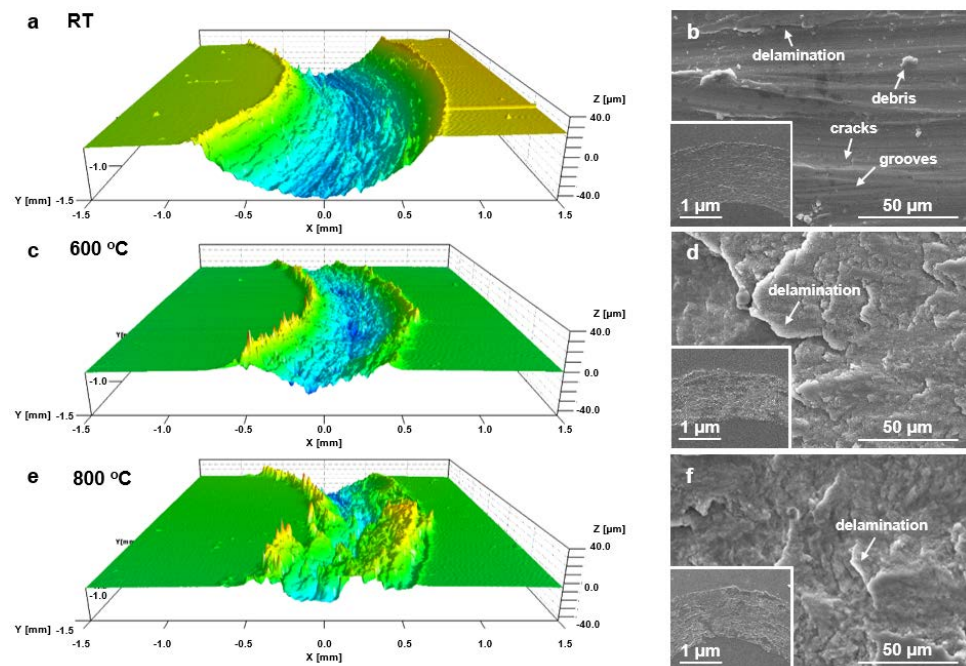


**Figure 4.** Wear surface profilometries of the FeCrNi MEA tested at (a) RT, (c)  $600^\circ\text{C}$  and (e)  $800^\circ\text{C}$ . The corresponding SE images are shown in (b,d,f), respectively.

**Table 1.** The chemical composition (at.%) of the different regions (marked in Figure 4) on the wear surfaces of the FeCrNi MEA.

Temperature ( $^\circ\text{C}$ )	Region	Fe	Cr	Ni	O
RT	Debris	22.6	27.7	21.1	28.6
-	Overall	25.5	30.9	23.7	19.9
600	Overall	16.1	18.8	15.1	50.0
800	Overall	14.8	17.7	14.7	52.8

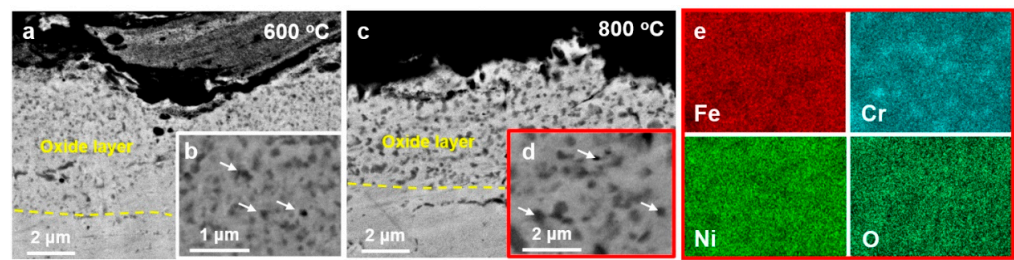


**Figure 5.** Cross-section morphologies of the wear surfaces for the FeCrNi MEA tested at (a,b) 600 °C and (c,d) 800 °C, and (e) the EDS mapping analysis inside the region marked in Figure 5d.

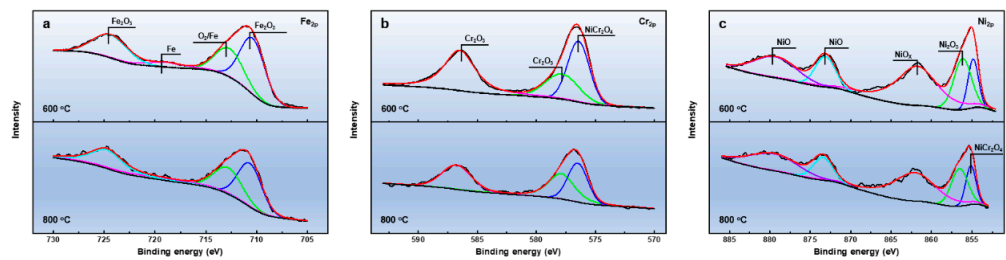


**Figure 6.** XPS spectra revealing the wear surface chemistry for the FeCrNi MEA tested at 600 °C and 800 °C. (a) Fe 2p, (b) Cr 2p and (c) Ni 2p.

In addition, the grain size of the subsurface layer is another factor that affects the high temperature wear resistance. High temperature wear is actually a thermomechanical deformation process, and dynamic recrystallization may occur on the wear subsurface, which leads to grain refinement. For example, dynamic recrystallized structures were observed in subsurface-deformed structures of the MEAs/HEAs such as CoCrFeMnNi and Al<sub>0.6</sub>CoCrFeNi under sliding wear conditions [23,26]. Dynamic recrystallization of high temperature wear subsurfaces of Hadfield steels has also been reported [23]. This phenomenon is usually caused by localized plastic deformation with large strain and frictional heat accumulation beneath the wear surface during dry sliding wear at high operating temperatures. In general, the grain size of dynamic recrystallization is closely related to temperature. Joseph et al. [23,26] studied the effect of temperature on the friction and wear behavior of CoCrFeMnNi. The results show a fine-grained structure in the wear subsurface at 600 °C, where CoCrFeMnNi exhibits the lowest wear rate. However, as the deformation temperature increases to 800 °C, the recrystallized microstructure becomes significantly coarser, which is mainly due to the positive correlation between diffusion and grain boundary mobility with temperature. At the same time, the grain size at 800 °C may also be affected by the growth of the second phase, because the pinning phenomenon caused by the second phase will be weakened at high temperature. As the result, the wear rate of the FeCrNi MEA increased slightly at 800 °C.

#### 4. Conclusions

In this work, a high Cr stainless FeCrNi MEA was prepared by powder metallurgy. The microstructure and the tribological properties of the FeCrNi MEA during dry sliding wear against Si<sub>3</sub>N<sub>4</sub> balls under various testing temperatures were investigated in detail. The main conclusions are as follows:

(1) The wear rate of the FeCrNi MEA decreases from RT to 600 °C and slightly increases afterwards at 800 °C, whereas the friction coefficient monotonously decreases with the increasing test temperatures.

(2) High Cr content in the FeCrNi MEA can promote the formation of compact oxide layer at intermediate temperature, which is beneficial to reduce wear adhesion and improve tribological performance. Consequently, the wear mechanism changes from abrasive wear to oxidative-delamination wear.

(3) In addition to the protection of the oxide layer, the precipitation of the hard  $\sigma$  phase induced by Cr element also plays a key role in improving the wear resistance of the FeCrNi MEA. This is mainly because the precipitates can effectively enhance the hardness of the oxide layer, thereby improving the wear resistance.

**Author Contributions:** A.F.: Methodology, Formal analysis, Writing—original draft. Z.X.: Investigation, Formal analysis. W.H.: Investigation, Writing—review & editing. Y.C.: Funding acquisition, Project administration, Formal analysis. All authors have read and agreed to the published version of the manuscript.

**Funding:** This study was financially supported by the Hubei Provincial Natural Science Foundation of China [No. 2022CFB894], the Science and Technology Project of Changsha [No. kh2203004] and the Open Project of Foshan (Southern China) Institute for New Materials [No. 2021AYF25010].

**Data Availability Statement:** The data presented in this study are available on request from the corresponding author.

**Conflicts of Interest:** The authors declare no conflict of interest.

## References

1. Atashin, S.; Pakshir, M.; Yazdani, A. Synergistic investigation into the marine parameters' effect on the corrosion rate of AISI 316 stainless steel. *Mater. Des.* **2011**, *32*, 1315–1324. [[CrossRef](#)]
2. Luo, H.; Li, Z.; Mingers, A.M.; Raabe, D. Corrosion behavior of an equiatomic CoCrFeMnNi high-entropy alloy compared with 304 stainless steel in sulfuric acid solution. *Corros. Sci.* **2018**, *134*, 131–139. [[CrossRef](#)]
3. Wang, L.; Seyeux, A.; Marcus, P. Thermal stability of the passive film formed on 316L stainless steel surface studied by ToF-SIMS. *Corros. Sci.* **2020**, *165*, 108395. [[CrossRef](#)]
4. Massoud, T.; Maurice, V.; Klein, L.H.; Marcus, P. Nanoscale morphology and atomic structure of passive films on stainless steel. *J. Electrochem. Soc.* **2013**, *160*, C232. [[CrossRef](#)]
5. Zhang, B.; Ma, X.L. A review—Pitting corrosion initiation investigated by TEM. *J. Mater. Sci. Technol.* **2019**, *35*, 1455–1465. [[CrossRef](#)]
6. Hsieh, C.C.; Wu, W. Overview of intermetallic sigma ( $\sigma$ ) phase precipitation in stainless steels. *ISRN Metall.* **2012**, *2012*, 1–16. [[CrossRef](#)]
7. Li, W.; Xie, D.; Li, D.; Zhang, Y.; Gao, Y.; Liaw, P.K. Mechanical behavior of high-entropy alloys. *Prog. Mater. Sci.* **2021**, *118*, 100777. [[CrossRef](#)]
8. Miracle, D.B.; Senkov, O.N. A critical review of high entropy alloys and related concepts. *Acta Mater.* **2017**, *122*, 448–511. [[CrossRef](#)]
9. George, E.P.; Raabe, D.; Ritchie, R.O. High-entropy alloys. *Nat. Rev. Mater.* **2019**, *4*, 515–534. [[CrossRef](#)]
10. Wu, Z.; Bei, H.; Otto, F.; Pharr, G.M.; George, E.P. Recovery, recrystallization, grain growth and phase stability of a family of FCC-structured multi-component equiatomic solid solution alloys. *Intermetallics* **2014**, *46*, 131–140. [[CrossRef](#)]
11. Wang, K.; Wang, X.; Zhang, T.; Jin, T.; Yang, H.; Qiao, J. Tuning Cr-rich nanoprecipitation and heterogeneous structure in equiatomic CrFeNi medium-entropy stainless alloys. *J. Iron Steel Res. Int.* **2022**, *29*, 529–536. [[CrossRef](#)]
12. Duan, H.; Liu, B.; Fu, A.; He, J.; Yang, T.; Liu, C.T.; Liu, Y. Segregation enabled outstanding combination of mechanical and corrosion properties in a FeCrNi medium entropy alloy manufactured by selective laser melting. *J. Mater. Sci. Technol.* **2022**, *99*, 207–214. [[CrossRef](#)]
13. Schneider, M.; Laplanche, G. Effects of temperature on mechanical properties and deformation mechanisms of the equiatomic CrFeNi medium-entropy alloy. *Acta Mater.* **2021**, *204*, 116470. [[CrossRef](#)]
14. Liang, D.; Zhao, C.; Zhu, W.; Wei, P.; Jiang, F.; Zhang, Y.; Sun, Q.; Ren, F. Overcoming the strength-ductility trade-off via the formation of nanoscale Cr-rich precipitates in an ultrafine-grained FCC CrFeNi medium entropy alloy matrix. *Mater. Sci. Eng. A* **2019**, *762*, 138107. [[CrossRef](#)]
15. Zhou, Z.; Liu, B.; Guo, W.; Fu, A.; Duan, H.; Li, W. Corrosion behavior and mechanism of FeCrNi medium entropy alloy prepared by powder metallurgy. *J. Alloy Compd.* **2021**, *867*, 159094. [[CrossRef](#)]
16. Fu, A.; Liu, B.; Lu, W.; Liu, B.; Li, J.; Fang, Q.; Li, Z.; Liu, Y. A novel supersaturated medium entropy alloy with superior tensile properties and corrosion resistance. *Scr. Mater.* **2020**, *186*, 381–386. [[CrossRef](#)]
17. Laplanche, G.; Kostka, A.; Reinhart, C.; Hunfeld, J.; Eggeler, G.; George, E.P. Reasons for the superior mechanical properties of medium-entropy CrCoNi compared to high-entropy CrMnFeCoNi. *Acta Mater.* **2017**, *128*, 292–303. [[CrossRef](#)]
18. Geng, Y.; Chen, J.; Tan, H.; Cheng, J.; Zhu, S.; Yang, J. Tribological performances of CoCrFeNiAl high entropy alloy matrix solid-lubricating composites over a wide temperature range. *Tribol. Int.* **2021**, *157*, 106912. [[CrossRef](#)]
19. Du, L.M.; Lan, L.W.; Zhu, S.; Yang, H.J.; Shi, X.H.; Liaw, P.K.; Qiao, J.W. Effects of temperature on the tribological behavior of Al<sub>0.25</sub>CoCrFeNi high-entropy alloy. *J. Mater. Sci. Technol.* **2019**, *35*, 917–925. [[CrossRef](#)]

20. Wang, Y.; Yang, Y.; Yang, H.; Zhang, M.; Ma, S.; Qiao, J. Microstructure and wear properties of nitrided AlCoCrFeNi high-entropy alloy. *Mater. Chem. Phys.* **2018**, *210*, 233–239. [[CrossRef](#)]
21. Gåård, A.; Krakhmalev, P.; Bergström, J.; Grytzeliuss, J.H.; Zhang, H.M. Experimental study of the relationship between temperature and adhesive forces for low-alloyed steel, stainless steel, and titanium using atomic force microscopy in ultrahigh vacuum. *J. Appl. Phys.* **2008**, *103*, 124301. [[CrossRef](#)]
22. Wu, J.M.; Lin, S.J.; Yeh, J.W.; Chen, S.K.; Huang, Y.S.; Chen, H.C. Adhesive wear behavior of Al<sub>x</sub>CoCrCuFeNi high-entropy alloys as a function of aluminum content. *Wear* **2006**, *261*, 513–519. [[CrossRef](#)]
23. Joseph, J.; Haghdadi, N.; Annasamy, M.; Kada, S.; Hodgson, P.D.; Barnett, M.R.; Fabijanic, D.M. On the enhanced wear resistance of CoCrFeMnNi high entropy alloy at intermediate temperature. *Scr. Mater.* **2020**, *186*, 230–235. [[CrossRef](#)]
24. Tian, X.; Zhang, Y.; Li, J. Investigation on tribological behavior of advanced high strength steels: Influence of hot stamping process parameters. *Tribol. Lett.* **2012**, *45*, 489–495. [[CrossRef](#)]
25. Jo, Y.H.; Choi, W.M.; Sohn, S.S.; Kim, H.S.; Lee, B.J.; Lee, S. Role of brittle sigma phase in cryogenic-temperature-strength improvement of non-equi-atomic Fe-rich VCrMnFeCoNi high entropy alloys. *Mater. Sci. Eng. A* **2018**, *724*, 403–410. [[CrossRef](#)]
26. Joseph, J.; Haghdadi, N.; Shamlaye, K.; Hodgson, P.; Barnett, M.; Fabijanic, D. The sliding wear behaviour of CoCrFeMnNi and Al<sub>x</sub>CoCrFeNi high entropy alloys at elevated temperatures. *Wear* **2019**, *428*, 32–44. [[CrossRef](#)]
27. Chen, M.; Lan, L.; Shi, X.; Yang, H.; Zhang, M.; Qiao, J. The tribological properties of Al<sub>0.6</sub>CoCrFeNi high-entropy alloy with the  $\sigma$  phase precipitation at elevated temperature. *J. Alloy Compd.* **2019**, *777*, 180–189. [[CrossRef](#)]

**Disclaimer/Publisher’s Note:** The statements, opinions and data contained in all publications are solely those of the individual author(s) and contributor(s) and not of MDPI and/or the editor(s). MDPI and/or the editor(s) disclaim responsibility for any injury to people or property resulting from any ideas, methods, instructions or products referred to in the content.